

# Assignment 2 – First-Principles Calculations of the Electronic Properties of Bulk Calcium Oxide

Sylvain Mortgat

April 13, 2025

## 1 Introduction to Density Functional Theory

### 1.1 Schrödinger $N$ -body Problem

In principle, to fully describe the physics of a solid made of electrons and ions, one should solve the time-independent Schrödinger equation

$$\hat{\mathcal{H}} |\psi\rangle = E |\psi\rangle, \quad (1)$$

with  $|\psi\rangle$  the state of the system,  $E$  the total energy, and  $\hat{\mathcal{H}} = \hat{T}_{e-e} + \hat{T}_{i-i} + \hat{V}_{e-e} + \hat{V}_{i-i} + \hat{V}_{e-i}$  the Hamiltonian composed of ionic and electronic kinetic terms as well as interaction terms. In the Born-Oppenheimer approximation, ions are treated as fixed and generate a static external potential  $\hat{V}$ . This simplifies the Hamiltonian to  $\hat{\mathcal{H}} = \hat{T} + \hat{U} + \hat{V}$ , where  $\hat{T}$  is the kinetic energy and  $\hat{U}$  is the electron-electron interaction energy. For a  $N$  electrons system, Equation 1 can be explicitly written as

$$\left[ \underbrace{-\frac{\hbar^2}{2m} \sum_{i=1}^N \frac{\partial^2}{\partial \vec{r}_i^2}}_{=\hat{T}} + \underbrace{\sum_{i=1}^N V(\vec{r}_i)}_{=\hat{V}} + \underbrace{\sum_{i<j}^N \frac{e^2}{\|\vec{r}_i - \vec{r}_j\|}}_{=\hat{U}} \right] \psi(\vec{r}_1, \dots, \vec{r}_N) = E \psi(\vec{r}_1, \dots, \vec{r}_N), \quad (2)$$

where  $\vec{r}_i$  are the positions of the electrons. The potential  $V(\vec{r}_i)$  created by all static ions (at positions  $\{\vec{R}_j\}$  and charge  $Z_j$ ) is given by

$$V(\vec{r}_i) = - \sum_j \frac{e^2 Z_j}{\|\vec{r}_i - \vec{R}_j\|}. \quad (3)$$

By solving Equation 2, i.e. by determining the wavefunction  $\psi$ , all relevant physical quantities can be derived. For instance the electronic density is given by

$$n(\vec{r}) = N \int d^3\vec{r}_2 \dots d^3\vec{r}_N \psi^*(\vec{r}, \dots, \vec{r}_N) \psi(\vec{r}, \dots, \vec{r}_N). \quad (4)$$

In practice, Equation 2 is impossible to solve analytically as  $N$  is typically of the order of  $10^{23}$ .

### 1.2 (Kohn-Sham) Density Functional Theory in a Nutshell

*Density Functional Theory* (DFT), is a framework that circumvents the difficulty of the initial problem by expressing all physically relevant quantities as functional of the electron density  $n(\vec{r})$ . Although this reformulation does not simplify the problem analytically, it renders the numerical solution much more feasible.

**Hohenberg-Kohn theorems** DFT is based on two theorems from Hohenberg and Kohn [1]. Their first theorem states that the non-degenerate ground state electron density  $n_0(\vec{r})$  determines the external potential  $\hat{V}$  to within a trivial additive constant. A direct consequence of this theorem is that the ground-state wave function can be written as a functional of the density:  $\psi_0 = \psi[n_0]$  [2]. Therefore, the ground-state energy, which is the expectation value of the Hamiltonian with respect to  $\psi_0$ , also becomes a functional of the density

$$\begin{aligned} E_0 \equiv E_0[n_0] &= \langle \psi_0 | \hat{\mathcal{H}} | \psi_0 \rangle \\ &= \langle \psi[n_0] | \hat{T} + \hat{V} + \hat{U} | \psi[n_0] \rangle \\ &= \langle \psi[n_0] | \hat{T} + \hat{U} | \psi[n_0] \rangle + \langle \psi[n_0] | \hat{V} | \psi[n_0] \rangle \\ &= \langle \psi[n_0] | \hat{T} + \hat{U} | \psi[n_0] \rangle + \int d^3\vec{r} V(\vec{r}) n_0(\vec{r}), \end{aligned} \quad (5)$$

where in the last step, a clear separation was made between universal terms ( $\hat{T}$  and  $\hat{U}$  have the same form regardless of the system) and the system-dependent term containing the external potential. Then, the second theorem states that *the ground state density can be determined from the ground state energy functional  $E[n] = \langle \psi[n] | \hat{\mathcal{H}} | \psi[n] \rangle$  via the variational principle, by variation of the density only*. In other words, given a trial density  $n$ , the ground state density  $n_0$  can be obtained by minimizing

$$E[n] = F[n] + \int d^3\vec{r} V(\vec{r}) n(\vec{r}) \geq E_0, \quad (6)$$

where the universal functional  $F[n] = \langle \psi[n] | \hat{T} + \hat{U} | \psi[n] \rangle = \hat{T}[n] + \hat{U}[n]$  is defined. Yet, the explicit form of  $F$  is not known.

**Khon-Sham equations** To make further progress, Khon and Sham proposed to map the problem of interacting electrons onto a non-interacting system ( $s$ ) of electrons with the same density [3]. Consider this auxiliary system  $s$  of  $N$  non-interacting electrons in an external potential  $\hat{V}_s(\vec{r})$ . The wavefunction can be written as a fully anti-symmetrized product of single-particle orbitals (Slater determinant), denoted  $\phi_i$ . Each one of these orbitals satisfy the single-particle Schrödinger equation:

$$\left[ -\frac{\hbar^2}{2m} \frac{\partial^2}{\partial \vec{r}^2} + \hat{V}_s(\vec{r}) \right] \phi_i(\vec{r}) = \epsilon_i \phi_i(\vec{r}). \quad (7)$$

As there are no interactions, the universal functional simplifies to

$$F_s[n] = \sum_{i=1}^N \left\langle \phi_i \left| -\frac{\hbar^2}{2m} \frac{\partial^2}{\partial \vec{r}^2} \right| \phi_i \right\rangle = \sum_{i=1}^N \int d^3\vec{r} \phi_i^*(\vec{r}) \left( -\frac{\hbar^2}{2m} \frac{\partial^2}{\partial \vec{r}^2} \right) \phi_i(\vec{r}) = T_s[n], \quad (8)$$

which shows that  $T_s[n]$  is itself a universal functional of the electron density. In this non-interacting case, the electron density is given by

$$n(\vec{r}) = \sum_{i=1}^N |\phi_i(\vec{r})|^2. \quad (9)$$

This relation between the density and the orbitals makes it possible to express the total energy functional in terms of the orbitals rather than directly as a density functional, i.e.  $E[n] \equiv E[\{\phi_i\}]$ . In the original system of interacting electrons, the universal functional can then be written as

$$F[n] = T_s[n] + E_H[n] + E_{xc}[n], \quad \text{with} \quad E_H[n] = \frac{e^2}{2} \int d^3\vec{r} d^3\vec{r}' \frac{n(\vec{r}) n(\vec{r}')}{\|\vec{r} - \vec{r}'\|}. \quad (10)$$

Here,  $E_H[n]$  represents the Coulomb (Hartree) interaction energy and  $E_{xc}[n]$  denotes the exchange-correlation energy. With these definitions, the total energy functional becomes

$$E[\{\phi_i\}] = \sum_{i=1}^N \int d^3\vec{r} \phi_i^*(\vec{r}) \left( -\frac{\hbar^2}{2m} \frac{\partial^2}{\partial \vec{r}^2} + V(\vec{r}) \right) \phi_i(\vec{r}) + E_H[n] + E_{xc}[n]. \quad (11)$$

By minimizing  $E[\{\phi_i\}]$  with respect to the spatial orbitals  $\phi_i(\vec{r})$  with the constraints of keeping the orbitals orthonormalized (see [4] for the derivation), one obtains the Kohn–Sham equations:

$$\hat{h}_{KS}\phi_i(\vec{r}) := \left[ -\frac{\hbar^2}{2m} \frac{\partial^2}{\partial \vec{r}^2} + V_{KS}(\vec{r}) \right] \phi_i(\vec{r}) = \epsilon_i \phi_i(\vec{r}), \quad (12)$$

where the effective Kohn–Sham potential is given by

$$V_{KS}(\vec{r}) = V(\vec{r}) + \int d^3\vec{r}' \frac{n(\vec{r}')}{\|\vec{r} - \vec{r}'\|} + \frac{\delta E_{xc}[n]}{\delta n(\vec{r})}. \quad (13)$$

The Kohn–Sham formulation represents an immense advantage as it decouples the Schrödinger equation into  $N$  independent equations.

**Self-consistent procedure** The standard approach to determine the ground state density is depicted in Figure 1. It begins with an initial trial density  $n^{(0)}(\vec{r})$ . From this, one first calculates the Kohn–Sham potential  $V_{KS}$  as described by Equation 13. Then, the orbitals  $\phi_i^{(0)}(\vec{r})$  are determined by solving the Kohn–Sham equations 12. These orbitals yield a new density

$$n^{(1)}(\vec{r}) = \sum_{i=1}^N |\phi_i^{(0)}(\vec{r})|^2. \quad (14)$$

This updated density serves as the input for the next iteration, where a new  $V_{KS}$  is computed, which yield new orbitals  $\phi_i^{(1)}(\vec{r})$  that determine  $n^{(2)}(\vec{r})$ , and so on. This procedure is repeated until self-consistency is reached, meaning that successive densities converge within a predefined tolerance.

**Decomposition in an orthogonal basis** In practical calculations, orbitals are decomposed in an orthogonal basis  $\{|\chi_\nu\rangle\}_{\nu=1}^M$ , i.e.

$$|\phi_i\rangle = \sum_{\nu=1}^M c_{\nu i} |\chi_\nu\rangle. \quad (15)$$

This allows to turn the Kohn–Sham differential Equation 12 into a matrix equation.

$$\hat{h}_{KS} |\phi_i\rangle = \epsilon_i |\phi_i\rangle \quad (16)$$

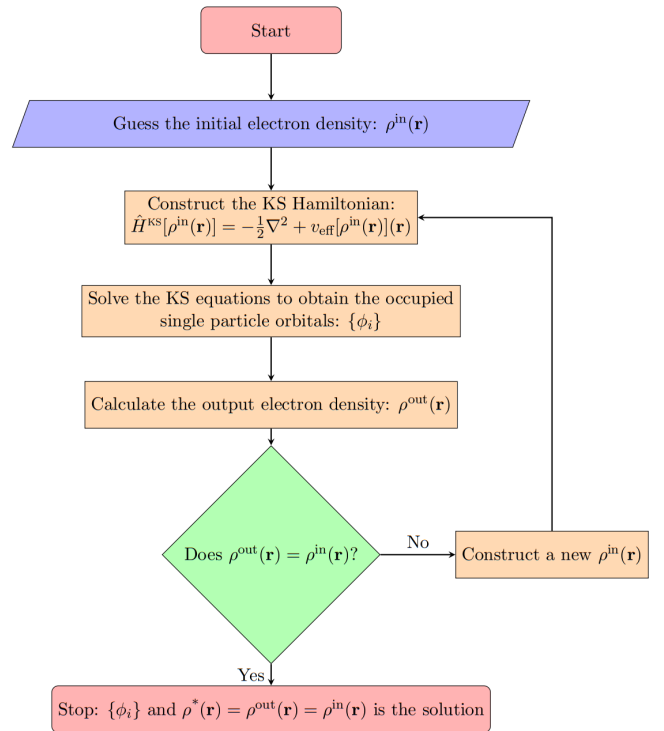


Figure 1: Self-consistent solution to the KS equations [5].

By expanding  $|\phi_i\rangle$  with Equation 15 and multiplying on the left by  $\langle\chi_\mu|$ , one obtains

$$\sum_{\nu=1}^M \langle\chi_\mu|\hat{h}_{\text{KS}}|\chi_\nu\rangle c_{\nu i} = \epsilon_i c_{\mu i}, \quad \forall \mu = 1, \dots, M, \quad (17)$$

which is equivalent, in matrix notation, to

$$\begin{pmatrix} \langle\chi_1|\hat{h}_{\text{KS}}|\chi_1\rangle & \cdots & \langle\chi_1|\hat{h}_{\text{KS}}|\chi_M\rangle \\ \vdots & \ddots & \vdots \\ \langle\chi_M|\hat{h}_{\text{KS}}|\chi_1\rangle & \cdots & \langle\chi_M|\hat{h}_{\text{KS}}|\chi_M\rangle \end{pmatrix} \begin{pmatrix} c_{1i} \\ \vdots \\ c_{Mi} \end{pmatrix} = \epsilon_i \begin{pmatrix} c_{1i} \\ \vdots \\ c_{Mi} \end{pmatrix} \quad (18)$$

or more concisely

$$\mathbf{h}_{\text{KS}} \vec{c}_i = \epsilon_i \vec{c}_i. \quad (19)$$

Therefore, within one iteration of the self-consistency calculation,  $N$  eigenvalue equations must be solved to determine the new trial density.

**Planewave basis** In a periodic solid, there is a particularly suitable choice for an orthogonal basis. This choice arises when the Hamiltonian is invariant under a translation by  $\vec{R}$ . In this setting, Bloch's theorem gives an explicit decomposition of orbitals into a phase factor and a periodic function of the lattice:

$$\phi_{n\vec{k}}(\vec{r}) = e^{i\vec{k}\cdot\vec{r}} u_{n\vec{k}}(\vec{r}), \quad \text{with} \quad u_{n\vec{k}}(\vec{r} + \vec{R}) = u_{n\vec{k}}(\vec{r}). \quad (20)$$

The integer  $n$  represents the band index and the vector  $\vec{k}$  represents crystal momentum, a quantity that is invariant under translation by a reciprocal lattice vector  $\vec{G}$ . Consequently, all the information about the wavefunctions is contained within a single region in reciprocal space, typically chosen as the first Brillouin zone. Since  $\phi_{n\vec{k}}$  is periodic in reciprocal space, it is natural to choose a basis with the same periodic behavior. The most popular basis expansion is in terms of *planewaves*:

$$\phi_{n\vec{k}}(\vec{r}) = e^{i\vec{k}\cdot\vec{r}} \left( \sum_{\vec{G}} c_{n\vec{k}}(\vec{G}) e^{i\vec{G}\cdot\vec{r}} \right) = \sum_{\vec{G}} c_{n\vec{k}}(\vec{G}) e^{i(\vec{k}+\vec{G})\cdot\vec{r}}, \quad (21)$$

for  $\vec{k}$  in the first Brillouin zone and  $\vec{G}$  a reciprocal vector.

**Energy cutoff** The planewave basis exhibits several advantages: planewaves are easy to differentiate, orthonormal, unbiased, and can take advantage of the Fast Fourier Transform algorithm due to the duality between real and reciprocal space [6]. The fact that there is no bias in the basis toward a particular input system implies that the accuracy of the planewave representation converges monotonically with increasing number of planewaves ordered by increasing magnitude of  $\vec{G}$  [5]. This remark is particularly useful, as it allows to truncate the planewave expansion by establishing a cutoff based on the norm of reciprocal vectors. In practical implementations, the cutoff is given in energy units  $E_{\text{cut}} := \hbar^2 G_{\text{cut}}^2 / (2m)$ , with  $m$  the electron mass and  $G_{\text{cut}}$  the cutoff reciprocal vector. The only terms that remain in Equation 21 are such that

$$\frac{\hbar^2 \|\vec{k} + \vec{G}\|^2}{2m} \leq E_{\text{cut}}. \quad (22)$$

Therefore, given a cutoff, orbitals are approximated as

$$\phi_{n\vec{k}}(\vec{r}) = \sum_{\|\vec{k}+\vec{G}\| \leq G_{\text{cut}}} c_{n\vec{k}}(\vec{G}) e^{i(\vec{k}+\vec{G})\cdot\vec{r}}. \quad (23)$$

Assuming that  $M$  reciprocal vectors satisfy the cutoff condition, upon relabeling ( $\{|\chi_\nu\rangle \equiv e^{i(\vec{k}+\vec{G}_\nu)\cdot\vec{r}}\}_{\nu=1}^M$ ,  $\{c_{\nu i} \equiv c_{\vec{n}\vec{k}}(\vec{G}_\nu)\}_{\nu=1}^M$  and  $\epsilon_i \equiv \epsilon_{\vec{n}\vec{k}}$ ), one finds an equation that is formally equivalent to Equation 18. Solving this eigenvalue problem determines the expansion coefficients  $\{c_{\vec{n}\vec{k}}(\vec{G}_\nu)\}$  which fully specify the Bloch wavefunctions  $\phi_{\vec{n}\vec{k}}(\vec{r})$ . The electron density is then computed by summing over occupied bands  $n$  and integrating over the Brillouin zone (BZ)

$$n(\vec{r}) = \frac{1}{V_{\text{BZ}}} \sum_n \int_{\text{BZ}} d^3\vec{k} |\phi_{\vec{n}\vec{k}}(\vec{r})|^2, \quad (24)$$

with  $V_{\text{BZ}}$  the volume of the Brillouin zone.

**Sampling of the Brillouin zone** Theoretically, Equation 24 requires integrating over an infinite number of  $\vec{k}$ -points in the Brillouin zone to perfectly reconstruct the electron density. However, this is computationally intractable in practice. In practice, the integral is approximated by a discrete sum over a finite set of  $\vec{k}$  vectors. A typical choice is the Monkhorst-Pack grid, which distributes  $\vec{k}$ -points uniformly across the Brillouin zone. This method reduces computational cost by exploiting the periodicity and symmetry of the system [7]. By applying symmetry operations, the full Brillouin zone can be reduced to the irreducible Brillouin zone, containing only those  $\vec{k}$ -points that are not equivalent under the symmetry of the crystal. This decreases the number of unique  $\vec{k}$ -points that must be explicitly sampled.

**Pseudo-potentials** When using the planewave basis, a significant computational challenge is that accurately representing localized electron states typically requires an impractically large number of plane waves. This is because localized electrons, especially those near the atomic core, exhibit rapid spatial oscillations. To address this, the *pseudo-potential approximation* leverages the observation that core electrons, i.e. those tightly bound near atomic nuclei, play a minimal direct role in determining a material's chemical or electronic properties. Instead, their primary influence lies in screening the nuclear charge experienced by valence electrons. Recognizing this, one can construct an effective potential that provides the exact behavior for valence electrons, without explicitly considering core electrons as degrees of freedom in the system. This approximation is depicted in Figure 2. The

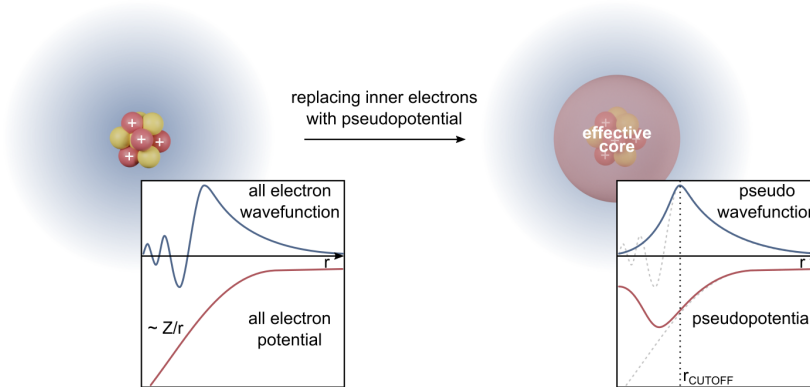


**Figure 2:** Schematic representation of the pseudo-potential approximation. The core potential is replaced by a smooth pseudo-potential. This allows the valence pseudo-wavefunctions to be represented with significantly fewer plane waves than all-electron wavefunctions [8].

pseudo-potential approximation can be implemented using two widely adopted formulations. *Norm-conserving pseudopotentials* enforce two main conditions: (1) the pseudo-wavefunction matches the corresponding all-electron wavefunction beyond a chosen cutoff radius  $r_c$ ; and (2) the integrated charge density (or “norm”) within  $r_c$  is preserved [9]. Despite these conditions, norm-conserving pseudopotentials remain “hard” in the sense that they require a large number of plane waves for

accurate representation. On the other hand, *ultrasoft pseudopotentials* relax the norm-conservation constraint to obtain significantly smoother pseudo-wavefunctions. In this approach, the pseudo-wavefunction is decomposed into two components: an ultrasoft valence wavefunction that may not conserve the norm (but still matches the all-electron wavefunction outside  $r_c$ ) and a set of augmentation charges that restore the correct localized charge within  $r_c$  [10]. This formulation allows a reduction in the required plane-wave cutoff energy.

**Quantum ESPRESSO implementation** *Quantum ESPRESSO* is an open-source computational framework for electronic-structure calculations based on density functional theory, plane-wave basis sets, and pseudopotentials [11]. It is widely used for materials modeling at the atomic scale. Quantum ESPRESSO employs atomic units where energy is expressed in Rydbergs and lengths in Bohr radii ( $a_{\text{Bohr}}$ ). In the present work, conversions from electronvolts to Rydbergs are frequently performed. The following reference values are used [12]:

$$1 \text{ Ry} = 13.605693122990(15) \text{ eV}, \quad \text{and} \quad 1 a_{\text{Bohr}} = 0.529177210544(82) \text{ \AA}. \quad (25)$$

In the simulations, an optimized norm-conserving Vanderbilt pseudo-potential is used [13].

## 2 Convergence of Energies, Forces and Energy Differences

Accurate DFT simulations require careful selection of computational parameters to ensure numerical reliability while avoiding unnecessary computational expense. This section determines appropriate kinetic energy cutoff  $E_{\text{cut}}$  and  $\vec{k}$ -point mesh density for subsequent calculations by converging three quantities: total energies, forces on displaced atoms and energy differences between CaO crystals with slightly different lattice parameters. The converged parameters established here will be directly applied in Section 3 for determining the equilibrium lattice constant, Section 4 for estimating the bulk modulus, and Section 5 for evaluating the elastic constants.

### 2.1 Definition of convergence

For any numerically computed physical quantity  $Q$  dependent on a control parameter  $\theta$  (e.g.,  $E_{\text{cut}}$  or  $\vec{k}$ -point density), convergence is operationalized through the following formalism. The hypothetical exact value obtained in the  $\theta \rightarrow \infty$  limit is denoted by  $Q_{\text{true}}$ . As this limit is computationally inaccessible, the reference value is defined as:

$$Q^* \equiv Q(\theta_{\text{max}}),$$

where  $\theta_{\text{max}}$  represents the maximum parameter value achievable within practical computational constraints. The convergence error is then quantified as:

$$\delta Q(\theta) = |Q(\theta) - Q^*|.$$

Convergence with respect to  $\theta$  is considered achieved when  $\delta Q(\theta) < T$ , where  $T$  is an accuracy threshold. To ensure robustness,  $Q(\theta)$  should approach  $Q^*$  monotonically near  $\theta_{\text{max}}$ .

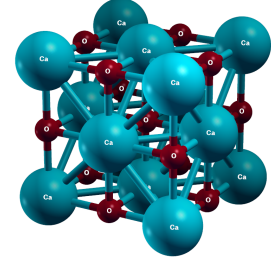
### 2.2 Convergence of Energies ( $E$ )

Here, the convergence behavior of the total energies is examined by varying both the kinetic energy cutoff and the  $\vec{k}$ -point mesh. Simulations are performed with the primitive cell instead of the conventional one to optimize computational efficiency. In this context, the use of the primitive cell is justified since the primary goal is to check the convergence of computed quantities rather than to extract detailed physical properties of the system. However, in Section 5, simulations are carried out using the conventional cell, as this facilitates the representation of strain effects on orthogonal lattice vectors, which is essential for determining the elastic constants.

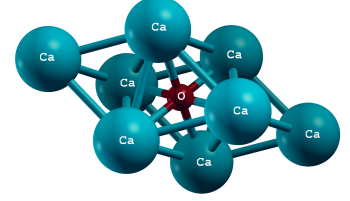


**Convergence with respect to  $E_{\text{cut}}$**  The CaO primitive cell, consisting of two atoms, is shown in Figure 3b. A  $4 \times 4 \times 4$   $\vec{k}$ -point grid is used for the calculations, and a convergence threshold of 5 meV per atom is defined. The energy per atom (calculated by dividing the total energy by two) is computed for cutoff energies values between 10 and 200 Ry in steps of 10 Ry, with 1000 Ry taken as the reference. As shown in Figure 4a, the convergence error  $\delta E$  falls below the threshold for  $E_{\text{cut}} = 80$  Ry  $\approx 1088$  eV. Beyond this value,  $\delta E$  continues to decrease monotonically, indicating sufficient convergence for subsequent calculations. This monotonic convergence is expected as discussed in Section 1.2.

**Convergence with respect to  $\vec{k}$  mesh** A  $\vec{k}$ -point mesh ranging from  $2 \times 2 \times 2$  to  $22 \times 22 \times 22$  in steps of  $2 \times 2 \times 2$  is examined, with a  $24 \times 24 \times 24$  mesh chosen as the reference. The converged value of  $E_{\text{cut}} = 80$  Ry is retained and the same 5 meV per atom threshold is applied. Figure 4b indicates that the convergence error remains below the threshold for  $k \geq 4$ . Although the error varies in a non-monotonic way, it stays many order of magnitudes below the threshold for  $k \geq 8$ . Figure 4c illustrates the efficacy of using symmetry operations when sampling the Brillouin zone. The ratio of the irreducible number of  $\vec{k}$ -points ( $\tilde{n}_k$ ) to the total number of  $\vec{k}$ -points ( $n_k$ ) decreases rapidly as the number the number of  $\vec{k}$ -points increases. This ratio reaches approximately 0.03 for  $k = 24$ , highlighting the significant reduction in computational effort achieved by exploiting symmetry operations.



(a)



(b)

**Figure 3:** CaO (a) conventional (b) primitive cell.

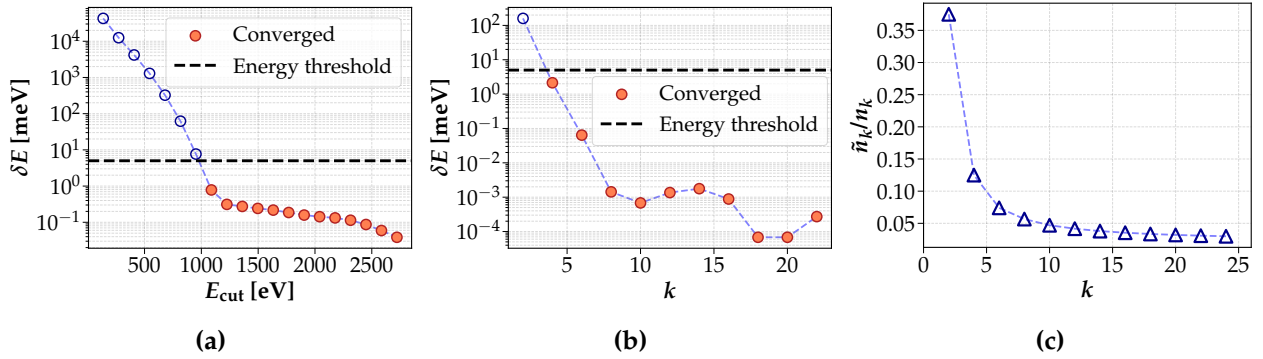


**Figure 4:** Convergence of total energies with respect to (a) the kinetic energy cutoff and (b) the  $\vec{k}$ -point mesh density. (c) Ratio of total to irreducible  $\vec{k}$ -points ( $\tilde{n}_k/n_k$ ) as a function of mesh density. A threshold of 5 meV per atom is applied for energy convergence in (a) and (b), with reference values set to  $E_{\text{cut}} = 1000$  Ry and  $k = 24$ .

### 2.3 Convergence of Forces ( $f_z$ )

The convergence of forces is investigated by displacing the Ca atom by 0.05 in fractional coordinates along the  $z$  direction inside the primitive cell. The resulting forces are analyzed with respect to variations in the kinetic energy cutoff and  $\vec{k}$ -point grid density.

**Convergence with respect to  $E_{\text{cut}}$**  A force convergence threshold of 10 meV/ $\text{\AA}$  is chosen using the same cutoff energies as in the energy convergence study. The same value of  $E_{\text{cut}} = 1000$  Ry is used as a reference to define the convergence error. A  $4 \times 4 \times 4$   $\vec{k}$ -point mesh containing the  $\Gamma$  point is also used for the computation. As shown in Figure 5a, the force error decreases almost exponentially

for the first seven cutoffs ( $E_{\text{cut}} \leq 70 \text{ Ry}$ ). Beyond this range, the error transitions to non-monotonic variations that oscillate around  $1 \text{ meV}/\text{\AA}$ . The first  $E_{\text{cut}}$  for which  $\delta f_z$  falls below the threshold is 50 Ry.

**Convergence with respect to  $\vec{k}$  mesh** The same force threshold of  $10 \text{ meV}/\text{\AA}$  is applied, with a reference  $\vec{k}$ -point mesh of  $16 \times 16 \times 16$ . A converged  $E_{\text{cut}}$  of 80 Ry is maintained while the  $\vec{k}$ -point grid density is varied between 2 and 14, in steps of 2. Figure 5b shows that the force error remains below the threshold for  $k \geq 4$ . The error decrease exhibits a quasi-monotonic behavior. The lowest convergence error is obtained for the largest grid, with  $k = 14$ .

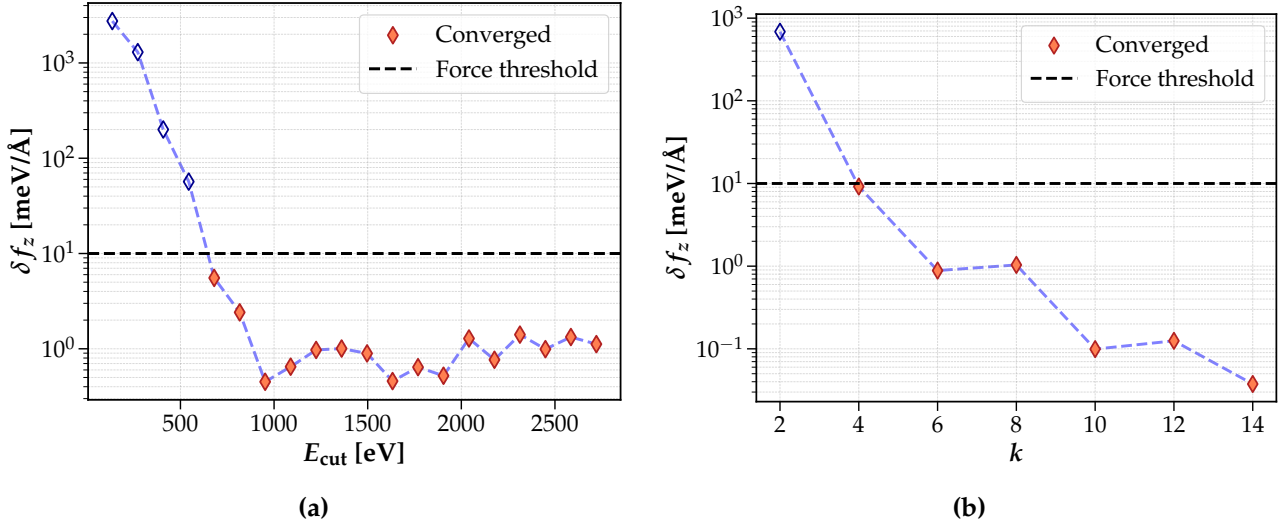


**Figure 5:** Convergence of forces with respect to (a) the kinetic energy cutoff and (b) the  $\vec{k}$ -point mesh density. A force threshold of  $10 \text{ meV}/\text{\AA}$  is applied, with reference values set to  $E_{\text{cut}} = 1000 \text{ Ry}$  and  $k = 16$ .

## 2.4 Convergence of Energy Differences ( $\Delta E$ )

In this section, the convergence behavior of the total energy difference between two CaO crystals with lattice parameters differing by 0.05 Bohr radii is analyzed with respect to the kinetic energy cutoff. To assess convergence, energy cutoffs are varied from 20 Ry to 100 Ry for three  $\vec{k}$ -point grids ( $k = 4, 6, 8$ ), with a reference cutoff of 1000 Ry. The convergence criterion is defined as an energy difference error below 5 meV per atom. Figure 6 illustrates the convergence behavior of the energy difference. For all  $\vec{k}$ -point grids, the error stabilizes beyond  $E_{\text{cut}} = 70 \text{ Ry}$ . Notably, grids with  $k = 6$  and 8 achieve convergence more rapidly than  $k = 4$ . Despite this stabilization, the error plateaus at  $5.08 \text{ meV}/\text{atom}$ , a value that slightly exceeds the predefined threshold. With these observations,  $E_{\text{cut}} = 70 \text{ Ry}$  seems to be an appropriate cutoff for energy difference calculations for any  $\vec{k}$ -point grid with  $k \geq 4$ .

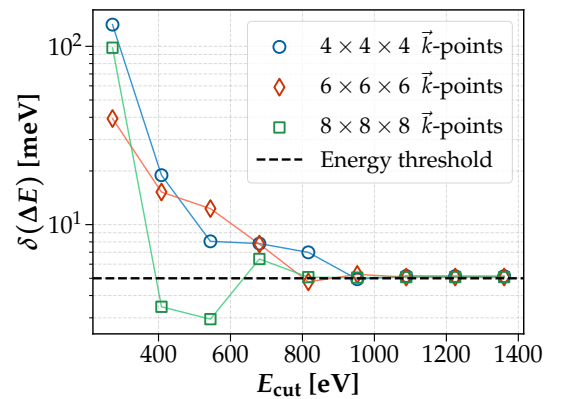


**Figure 6:** Convergence of total energy differences between CaO crystals with varying lattice parameters as a function of the energy cutoff. Results from different  $\vec{k}$ -point grids show that convergence is achieved around  $E_{\text{cut}} \approx 1000 \text{ eV}$ . Although  $\delta(\Delta E)$  remains above the  $5 \text{ meV/atom}$  threshold, no further precision is gained by increasing  $E_{\text{cut}}$  beyond this point. This indicates a stable converged state.



## 2.5 Summary of convergence cutoffs

Table 1 summarizes the convergence results obtained for total energies, forces and total energy differences. It highlights a hierarchy in kinetic energy cutoff: forces require the lowest one, followed by energy differences and total energies. Since forces are energy derivatives, error cancellations often happen in their calculation, resulting in a faster convergence. All three quantities achieve convergence with a  $4 \times 4 \times 4$   $\vec{k}$ -point mesh.

| Quantity           | $E_{\text{cut}}$ [Ry] | $\vec{k}$ -point Mesh |
|--------------------|-----------------------|-----------------------|
| Total Energy       | 80                    | 4                     |
| Forces             | 50                    | 4                     |
| Energy Differences | 70                    | 4                     |

**Table 1:** Converged computational parameters for CaO bulk properties. The kinetic energy cutoff  $E_{\text{cut}}$  and  $\vec{k}$ -point mesh density  $k_{\text{cut}}$  were determined using thresholds of 5 meV/atom for energies and 10 meV/Å for forces.

To define appropriate convergence cutoffs, note that the focus of the subsequent sections is not on the absolute computed energies, but on the energy differences between systems. In practice, properties such as the equilibrium lattice constant, bulk modulus, and elastic constants are determined by analyzing energy differences rather than the absolute energies. Based on these observations, we adopt the following convergence parameters for subsequent calculations:

$$E_{\text{cut}} = 70 \text{ Ry} \quad \text{and} \quad \vec{k}\text{-point grid of } 4 \times 4 \times 4.$$

**Switching to ultrasoft pseudo-potentials** Switching from norm-conserving to ultrasoft pseudo-potentials would alter convergence behavior since the pseudo-wavefunctions are typically smoother and less localized. Therefore they need less plane waves to be accurately approximated. However, because ultrasoft pseudo-potentials correct the charge deficit near the nuclei with augmentation charges, an additional cutoff parameter must be introduced and converged. This typically involves a higher cutoff for the augmentation charge density than for the wavefunctions themselves. Consequently, although a lower kinetic energy cutoff may suffice for the wavefunction expansion, a systematic convergence test must now also be performed on the augmentation charge cutoff to ensure that energy differences, forces, and other computed properties reach the desired accuracy.

## 3 Lattice parameter

The equilibrium lattice parameter of CaO is determined by finding the minima of the total energy over a range of primitive cell volumes. From this equilibrium volume  $V_0$ , the corresponding lattice parameter  $a_0$  is derived and then compared with both theoretical and experimental values. The lattice parameter will be important in Section 4 to determine the bulk modulus and in Section 5 to estimate the elastic constants  $C_{11}$ ,  $C_{12}$  and  $C_{44}$ .

**Methodology** To determine the equilibrium lattice constant of CaO, a series of simulations is performed. The calculations are carried out using a plane-wave basis set with an energy cutoff of 70 Ry, and a  $\vec{k}$ -point grid of  $4 \times 4 \times 4$  to sample the Brillouin zone. Lattices are initialized with lattice constants  $a$  ranging from 8 to 10 Bohr radii. Energy computations are initially carried out with a 0.05 Bohr radii step size, and near the energy minimum, a finer step size of 0.005 Bohr radii is used to gain in precision.

**Results** Figure 7 illustrates the total energy as a function of the primitive cell volume for CaO ( $V = a^3/4$ ). The curve exhibits a well-defined minimum at  $V_0 = (28.06 \pm 0.05) \text{ \AA}^3$ , corresponding to a lattice parameter of  $a_0 = (4.823 \pm 0.003) \text{ \AA}$ . The uncertainty in  $a_0$ , denoted by  $\delta a_0$ , is taken as half the refined step-size. The corresponding error in the volume is then obtained via error propagation as  $\delta V_0 = (\partial V_0 / \partial a_0) \delta a_0 = 3a_0^2 \delta a_0 / 4$ . The minimum in the total energy identifies the most stable configuration of CaO under the chosen computational conditions (plane-wave cutoff and  $\vec{k}$ -mesh). The computed equilibrium lattice parameter shows good agreement with both theoretical and experimental values reported in the literature. Table 2 summarizes the comparison with various references, revealing relative errors ranging from 0.08% to 0.8%. Notably, the computed value aligns closely with the one obtained by Fiquet et al. through X-ray diffraction experiments with synchrotron radiation [14]. These comparisons validate the accuracy of the computational approach employed.

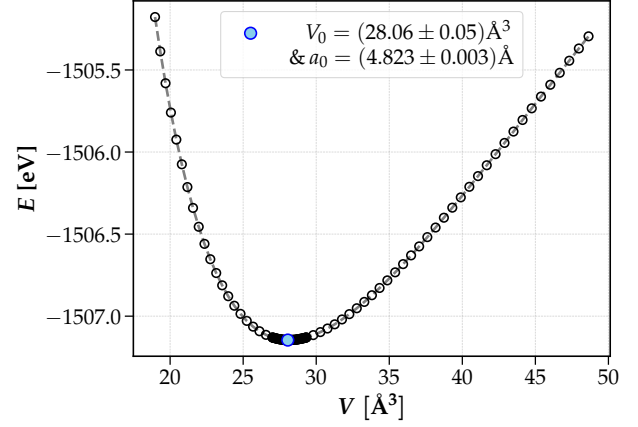


**Figure 7:** Total energy as a function of primitive cell volume for CaO. The equilibrium volume is  $V_0 = (28.06 \pm 0.05) \text{ \AA}^3$  and the corresponding lattice parameter is  $a_0 = (4.823 \pm 0.003) \text{ \AA}$ .

| Source                            | Lattice Constant [ $\text{\AA}$ ] | Relative Error [%] |
|-----------------------------------|-----------------------------------|--------------------|
| Fiquet et al. (EDXRD) [14]        | $4.81 \pm 0.01$                   | 0.3                |
| Liu et al. (PP-PAW-GGA) [15]      | 4.84                              | 0.4                |
| Habas et al. (PP-DFT-PBE) [16]    | 4.86                              | 0.8                |
| Marinelli et al. (PP-DFT-PW) [17] | 4.817                             | 0.12               |
| Aguado et al. (DFT-GGA-MD) [18]   | 4.809                             | 0.3                |
| Deng et al. (DFT-GGA) [19]        | 4.810                             | 0.3                |
| Albuquerque et al. (DFT-GGA) [20] | 4.819                             | 0.08               |

**Table 2:** Comparison of the computed lattice parameter  $a_0 = (4.823 \pm 0.003) \text{ \AA}$  with reference values.

## 4 Bulk Modulus

The bulk modulus of CaO, denoted  $B_0$ , is determined by analyzing the pressure–volume behavior derived from total-energy calculations at various cell volumes. In Section 4.1, it is estimated with a second-order approximation. In Section 4.2, a more refined calculation is performed by fitting the Birch-Murnaghan isothermal equation of state [21] around the equilibrium lattice constant obtained in Section 3.

### 4.1 Second-Order Approximation

The bulk modulus measures the resistance of a material to compression. It is defined as

$$B_0 = -V_0 \left. \frac{\partial P}{\partial V} \right|_{V=V_0}, \quad (26)$$

where  $P$  is the pressure on the material,  $V$  is its volume, and  $V_0$  is its equilibrium volume. The simplest approach to estimate  $B_0$  is to approximate the energy-volume relationship to second order

around the equilibrium configuration with energy  $E_0 \equiv E(V_0)$

$$E(V) \simeq E_0 + (V - V_0) \left. \frac{\partial E}{\partial V} \right|_{V=V_0} + \frac{1}{2} (V - V_0)^2 \left. \frac{\partial^2 E}{\partial V^2} \right|_{V=V_0}. \quad (27)$$

The first derivative vanishes as  $E(V_0)$  is the global minima, and the second derivative can be rewritten in terms of pressure as  $P = -\partial E / \partial V$

$$E(V) \simeq E_0 + \frac{1}{2} (V - V_0)^2 \left( - \left. \frac{\partial P}{\partial V} \right|_{V=V_0} \right) \stackrel{\text{Eq. 26}}{=} E_0 + \frac{1}{2} (V - V_0)^2 \frac{B_0}{V_0}. \quad (28)$$

By defining  $\Delta V = V - V_0$  and  $\Delta E(V) = E(V) - E_0$ , and letting  $\eta = \frac{B_0}{2V_0}$ , the above equation can be rewritten in quadratic form as:

$$\Delta E = \eta v^2. \quad (29)$$

Thus, by fitting a quadratic function to the data, the optimal parameter  $\hat{\eta}$  can be determined, which then allows for the evaluation of the bulk modulus as

$$B_0 = 2V_0 \hat{\eta}. \quad (30)$$

In practice,  $\hat{\eta}$  is determined by performing a nonlinear least-squares fit using the LMFIT library [22]. The uncertainty in this estimate is reported as 95% confidence intervals.

#### 4.2 Third-Order Birch-Murnaghan Isothermal Equation of State

The bulk modulus is then estimated by fitting the Birch-Murnaghan isothermal equation of state around the equilibrium lattice constant:

$$E(V) = E_0 + \frac{9}{8} B_0 V_0 \left[ \left( \frac{V_0}{V} \right)^{2/3} - 1 \right]^2 + \frac{9}{16} B_0 V_0 (B'_0 - 4) \left[ \left( \frac{V_0}{V} \right)^{2/3} - 1 \right]^3. \quad (31)$$

Here,  $B_0$  is the bulk modulus,  $B'_0$  its derivative,  $V$  the cell volume,  $V_0$  the equilibrium volume, and  $E_0$  the equilibrium energy. The parameters  $B_0$ ,  $B'_0$ ,  $V_0$ , and  $E_0$  are determined by performing a nonlinear least-squares fit using the LMFIT library [22]. The uncertainties in these estimates are reported as a 95% confidence interval.

#### 4.3 Results

Figure 8 displays the performed fits for the second-order approximation (Fig. 8a) and for the Birch-Murnaghan isothermal equation of state (Fig. 8b). All the data comes from Section 3 where the optimal (equilibrium) cell volume and lattice constant were found. For the quadratic approximation the optimized parameter is  $\hat{\eta} = (11.8 \pm 0.2) \text{ meV}/\text{\AA}^3$  which leads to  $B_0 = (106.3 \pm 1.9) \text{ GPa}$ . For the Birch-Murnaghan isothermal equation of state, the bulk modulus is directly estimated as  $\hat{B}_0 = (657.85 \pm 0.15) \text{ meV}/\text{\AA}^3 = (105.399 \pm 0.010) \text{ GPa}$ . The quadratic approximation shows larger uncertainty because it only captures the harmonic region near equilibrium. This simplified EOS approach misses the asymmetry in the energy-volume relationship (Fig. 7). The Birch-Murnaghan EOS provides better precision by accounting for anharmonic effects through higher-order terms. Its fit spans a broader volume range, reducing uncertainty. Despite these differences, both methods agree within approximately 1 GPa. The bulk modulus  $\hat{B}_0$  aligns reasonably with theoretical and experimental values (see Table 3). A relative error of 4% is observed with the radial X-ray diffraction (XRD) value of  $(110 \pm 5) \text{ GPa}$  obtained by Speziale et al. [23]. The computed value falls within the experimental uncertainty range. The variations observed for the other references likely arise from differences in computational approximations (e.g., exchange-correlation functionals) or experimental conditions (e.g., temperature effects).

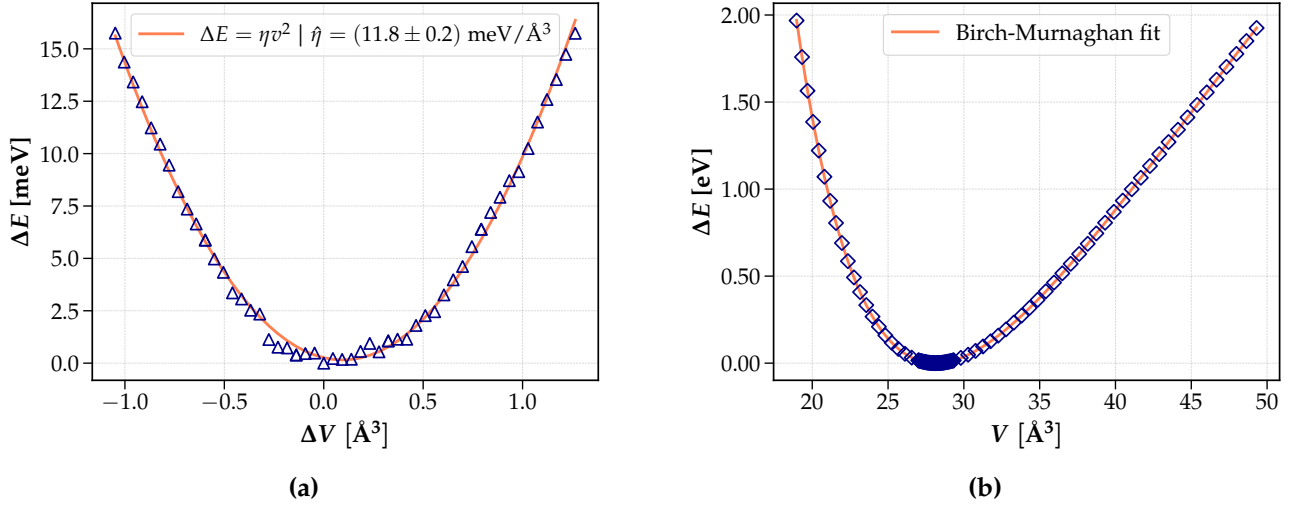


**Figure 8:** Determination of the bulk modulus for CaO. **(a)** Quadratic fit of the energy-volume relationship near equilibrium, where the curvature  $\hat{\eta}$  of the parabola directly gives  $B_0 = 2V_0\hat{\eta}$ . **(b)** Birch-Murnaghan isothermal equation of state fit, which incorporates higher-order anharmonic effects and provides a more robust estimate of  $B_0$ . Both methods use the equilibrium volume  $V_0$  obtained from total-energy calculations (Section 3).

| Source                                      | Bulk Modulus [GPa] | Relative Error [%] |
|---|--------------------|--------------------|
| Marinelli et al. (PP-DFT-PW) [17]           | 111                | 5                  |
| Aguado et al. (DFT-GGA-MD) [18]             | 116.1              | 9                  |
| Deng et al. (DFT-GGA) [19]                  | 111.99             | 6                  |
| Speziale et al. (Brillouin Scattering) [23] | $112.0 \pm 0.2$    | 6                  |
| Speziale et al. (XRD) [23]                  | $110 \pm 5$        | 4                  |

**Table 3:** Comparison of the computed bulk modulus  $\hat{B}_0 = (105.399 \pm 0.010)$  GPa with reference values.

## 5 Elastic Constants

The mechanical properties of crystalline solids are intimately connected to their elastic constants, which describe how the crystal responds to small deformations. The elastic constants  $C_{\alpha\beta}$  can be determined by applying small, controlled strains to the lattice and examining the resulting changes in total energy. In this exercise, we focus on computing  $C_{11}$ ,  $C_{12}$  and  $C_{44}$  for CaO by using a conventional cubic unit cell containing 8 atoms. By distorting the lattice according to specific symmetry constraints and performing energy calculations, we obtain the required elastic constants from the strain–energy relationship.

### 5.1 Elastic Constants

In the linear theory of elasticity, Hooke’s law relates the applied strain to the resulting stress. Both quantities are represented as rank-2 tensors,  $\hat{\varepsilon}$  for strain and  $\hat{\sigma}$  for stress. Components of these tensors are related through

$$\sigma_{ij} = \sum_{kl} C_{ijkl} \varepsilon_{kl}, \quad i, j, k, \ell \in \{x, y, z\} \quad (32)$$

with  $C_{ijkl}$  the components of the elasticity tensor. Due to symmetries of  $\hat{\varepsilon}$  and  $\hat{\sigma}$ , the elasticity tensor only has 21 independent components in general. Using the Voigt notation for a symmetric tensor,

Equation 32 can be written as

$$\sigma_\alpha = \sum_{\beta=1}^6 C_{\alpha\beta} e_\beta, \quad \alpha, \beta \in \{1, 2, 3, 4, 5, 6\} \quad (33)$$

with the convention  $xx \rightarrow 1$ ,  $yy \rightarrow 2$ ,  $zz \rightarrow 3$ ,  $yz \rightarrow 4$ ,  $zx \rightarrow 5$  and  $xy \rightarrow 6$ . For a system with cubic symmetry, the number of independent components of  $\mathbf{C}$  reduces to 3, conventionally denoted in normal font as  $C_{11}$ ,  $C_{12}$ , and  $C_{44}$  [24]. In particular,

$$\begin{cases} C_{11} = C_{11} = C_{22} = C_{33} \\ C_{12} = C_{12} = C_{21} = C_{13} = C_{31} = C_{23} = C_{32} \\ C_{44} = C_{44} = C_{55} = C_{66} \end{cases}.$$

With these definitions, the elasticity tensor for a cubic system is

$$\mathbf{C} = \begin{pmatrix} C_{11} & C_{12} & C_{12} & 0 & 0 & 0 \\ C_{12} & C_{11} & C_{12} & 0 & 0 & 0 \\ C_{12} & C_{12} & C_{11} & 0 & 0 & 0 \\ 0 & 0 & 0 & C_{44} & 0 & 0 \\ 0 & 0 & 0 & 0 & C_{44} & 0 \\ 0 & 0 & 0 & 0 & 0 & C_{44} \end{pmatrix}. \quad (34)$$

## 5.2 Lattice Response to a Volume-Conserving Strain

A volume-conserving strain is applied to the lattice. It induces a transformation of the equilibrium lattice vectors  $(\vec{a}_1, \vec{a}_2, \vec{a}_3)$  that transform to  $(\vec{a}'_1, \vec{a}'_2, \vec{a}'_3)$  through the following equation:

$$\begin{pmatrix} \vec{a}'_1 \\ \vec{a}'_2 \\ \vec{a}'_3 \end{pmatrix} = \begin{pmatrix} \vec{a}_1 \\ \vec{a}_2 \\ \vec{a}_3 \end{pmatrix} (\hat{\mathbf{1}} + \hat{\varepsilon}) = \begin{pmatrix} \vec{a}_1 \\ \vec{a}_2 \\ \vec{a}_3 \end{pmatrix} + \begin{pmatrix} \vec{a}_1 \\ \vec{a}_2 \\ \vec{a}_3 \end{pmatrix} \hat{\varepsilon}, \quad (35)$$

with  $\hat{\mathbf{1}}$  and  $\hat{\varepsilon}$  the identity and strain tensor, respectively. In terms of components, Equation 35 can be written as

$$\begin{pmatrix} a'_{1x} & a'_{1y} & a'_{1z} \\ a'_{2x} & a'_{2y} & a'_{2z} \\ a'_{3x} & a'_{3y} & a'_{3z} \end{pmatrix} = \begin{pmatrix} a_{1x} & a_{1y} & a_{1z} \\ a_{2x} & a_{2y} & a_{2z} \\ a_{3x} & a_{3y} & a_{3z} \end{pmatrix} + \begin{pmatrix} a_{1x} & a_{1y} & a_{1z} \\ a_{2x} & a_{2y} & a_{2z} \\ a_{3x} & a_{3y} & a_{3z} \end{pmatrix} \underbrace{\begin{pmatrix} e_1 & e_6/2 & e_5/2 \\ e_6/2 & e_2 & e_4/2 \\ e_5/2 & e_4/2 & e_3 \end{pmatrix}}_{=:\hat{\varepsilon}}. \quad (36)$$

Since the lattice moves away from equilibrium, its energy increases by an amount  $\Delta E$  given by

$$\Delta E = \frac{1}{2} V_0 \sum_{\alpha=1}^6 \sum_{\beta=1}^6 C_{\alpha\beta} e_\alpha e_\beta, \quad (37)$$

where  $V_0 = a_0^3$  denotes the equilibrium conventional cell volume.

## 5.3 Determination of the Elastic Constants

**Orthorhombic symmetry** To determine  $C_{11}$  and  $C_{12}$ , a tetragonal strain is applied to the system:

$$\hat{\varepsilon} = \begin{pmatrix} e_1 & 0 & 0 \\ 0 & e_2 & 0 \\ 0 & 0 & e_3 \end{pmatrix} = \begin{pmatrix} x & 0 & 0 \\ 0 & -x & 0 \\ 0 & 0 & \frac{x^2}{1-x^2} \end{pmatrix}, \quad (38)$$

which is initially cubic, i.e. the initial lattice vectors are  $\vec{a}_1 = a_0\vec{e}_x$ ,  $\vec{a}_2 = a_0\vec{e}_y$  and  $\vec{a}_3 = a_0\vec{e}_z$ . In matrix notation, plugging these into Equation 36 gives

$$\begin{pmatrix} \vec{a}'_1 \\ \vec{a}'_2 \\ \vec{a}'_3 \end{pmatrix} = a_0\hat{1} + a_0\hat{1} \begin{pmatrix} x & 0 & 0 \\ 0 & -x & 0 \\ 0 & 0 & \frac{x^2}{1-x^2} \end{pmatrix} = a_0 \begin{pmatrix} 1+x & 0 & 0 \\ 0 & 1-x & 0 \\ 0 & 0 & 1+\frac{x^2}{1-x^2} \end{pmatrix}. \quad (39)$$

Each lattice vector is only scaled with a multiplicative factor, without changing direction. The system becomes orthorhombic. The corresponding change in energy is obtained from Equation 37

$$\begin{aligned} \Delta E &= \frac{1}{2} V_0 (C_{11}e_1^2 + C_{22}e_2^2 + C_{33}e_3^2 + 2C_{12}e_1e_2 + 2C_{13}e_1e_3 + 2C_{23}e_2e_3) \\ &= \frac{1}{2} V_0 [C_{11}(e_1^2 + e_2^2 + e_3^2) + 2C_{12}(e_1e_2 + e_1e_3 + e_2e_3)] \\ &= \frac{1}{2} V_0 \left[ C_{11} \left( 2x^2 + \frac{x^4}{(1-x^2)^2} \right) - 2C_{12}x^2 \right] \\ &= V_0 [C_{11} - C_{12}]x^2 + o(x^4) \\ &\simeq \alpha x^2, \end{aligned} \quad (40)$$

where in the last step, the constant  $\alpha = V_0(C_{11} - C_{12})$  is defined and the fourth order contribution is neglected because  $x$  is assumed to be sufficiently small<sup>1</sup>. This formulation clearly shows that the energy variation is quadratic in the strain parameter. If  $\alpha$  can be accurately estimated, then the elastic constants  $C_{11}$  and  $C_{12}$  can be determined from their relationship with the bulk modulus  $B_0$ , which are given by

$$\begin{cases} \alpha = V_0(C_{11} - C_{12}) \\ B_0 = \frac{1}{3}(C_{11} + 2C_{12}) \end{cases} \Rightarrow \begin{cases} C_{11} = \frac{\alpha}{V_0} + C_{12} \\ B_0 = \frac{1}{3} \left( \frac{\alpha}{V_0} + C_{12} + 2C_{12} \right) \end{cases} \Rightarrow \begin{cases} C_{11} = B_0 + \frac{2}{3} \frac{\alpha}{V_0} \\ C_{12} = B_0 - \frac{1}{3} \frac{\alpha}{V_0} \end{cases}. \quad (41)$$

**Monoclinic Bravais lattice** To determine  $C_{44}$ , another tetragonal strain is applied to the system:

$$\hat{\varepsilon} = \begin{pmatrix} 0 & e_6/2 & 0 \\ e_6/2 & 0 & 0 \\ 0 & 0 & e_3 \end{pmatrix} = \begin{pmatrix} 0 & x/2 & 0 \\ x/2 & 0 & 0 \\ 0 & 0 & \frac{x^2}{4-x^2} \end{pmatrix}. \quad (42)$$

The transformation of the lattice vectors is obtained by applying Equation 36:

$$\begin{pmatrix} \vec{a}'_1 \\ \vec{a}'_2 \\ \vec{a}'_3 \end{pmatrix} = a_0\hat{1} + a_0\hat{1} \begin{pmatrix} 0 & x/2 & 0 \\ x/2 & 0 & 0 \\ 0 & 0 & \frac{x^2}{4-x^2} \end{pmatrix} = a_0 \begin{pmatrix} 1 & x/2 & 0 \\ x/2 & 1 & 0 \\ 0 & 0 & 1 + \frac{x^2}{4-x^2} \end{pmatrix}. \quad (43)$$

In this case, the strain tensor introduces an off-diagonal shear in the in the  $xy$  plane and simultaneously causes an elongation along the  $z$  direction. As a result, the transformed lattice becomes monoclinic, characterized by three different lattice constants and one angle:

$$\begin{cases} \|\vec{a}'_1\| = \|a_0(\vec{e}_x + \frac{x}{2}\vec{e}_y)\| = a_0\sqrt{1 + \frac{x^2}{4}} \\ \|\vec{a}'_2\| = \|a_0(\frac{x}{2}\vec{e}_x + \vec{e}_y)\| = a_0\sqrt{1 + \frac{x^2}{4}} \\ \|\vec{a}'_3\| = \|a_0(1 + \frac{x^2}{4-x^2})\vec{e}_z\| = a_0(1 + \frac{x^2}{4-x^2}) \\ \cos \theta = \frac{\vec{a}'_1 \cdot \vec{a}'_2}{\|\vec{a}'_1\| \|\vec{a}'_2\|} = \frac{a_0^2 x}{a_0^2(1 + \frac{x^2}{4})} = \frac{4x}{4 + x^2} \end{cases}. \quad (44)$$

<sup>1</sup> In the simulations, the strain parameter is restricted to  $x \in [0, 0.1]$ . For the maximum value  $x = 0.1$ , the ratio of the quadratic term to the quartic term, is approximately  $196 \gg 1$ . This justifies the neglect of the fourth-order contribution.



The energy variation is again obtained from Equation 37

$$\begin{aligned}\Delta E &= \frac{1}{2}V_0(C_{33}e_3^2 + C_{66}e_6^2) = \frac{1}{2}V_0(C_{11}e_3^2 + C_{44}e_6^2) = \frac{1}{2}V_0\left(C_{11}\frac{x^4}{(4-x^2)^2} + C_{44}x^2\right) \\ &= \frac{1}{2}V_0C_{44}x^2 + o(x^4) \\ &\simeq \beta x^2,\end{aligned}\tag{45}$$

where in the last step,  $\beta = V_0C_{44}/2$  is defined and the fourth order contribution is neglected. As in the orthorhombic case, the energy variation with respect to the strain parameter is quadratic. An accurate estimate of  $\beta$  directly provides an estimate of  $C_{44}$ :

$$\beta = \frac{1}{2}V_0C_{44} \implies C_{44} = \frac{2\beta}{V_0}.\tag{46}$$

**Estimating  $\alpha$  and  $\beta$**  It is now clear that the key point to determine the elastic constants is to make accurate estimates of  $\alpha$  and  $\beta$ . For  $\alpha$ , the orthorhombic geometry described in Equation 39 is implemented and energy minimization is calculated for  $x \in \{0, 0.01, 0.02, 0.03, 0.04, 0.05, 0.06, 0.07, 0.08, 0.09, 0.10\}$ , with an energy cutoff of 70 Ry and a  $\vec{k}$ -points grid of  $4 \times 4 \times 4$ . The equilibrium lattice constant is set to  $a_0 = 4.82 \text{ \AA}$ . The same procedure is conducted for  $\beta$  where the monoclinic lattice is implemented with Equations 43 and 44. For both geometries, the energy variation is quadratic and therefore symmetric about the strain parameter  $x = 0$ , i.e.,  $\Delta E(x) = \Delta E(-x)$ . This symmetry allows to double the number of effective measurements by extending the data to the interval  $[-0.1, 0.1]$  instead of being confined to  $[0, 0.1]$ . To estimate  $\alpha$  and  $\beta$ , a non-linear least square regression is performed with the LMFIT library [22]. The uncertainties in these estimates are reported as 95% confidence intervals.

**Results** Figure 9 displays the performed parabolic fits for both deformation modes. In panel 9a, the fit to the tetragonal deformation data yields  $\hat{\alpha} = (119.1 \pm 2.4) \text{ eV}$ . Panel 9b shows the corresponding fit for the monoclinic deformation, from which the parameter associated with  $C_{44}$  is estimated as  $\hat{\beta} = (26.91 \pm 0.05) \text{ eV}$ . With these values,  $V_0 = a_0^3$  and the bulk modulus determined in Section 4,  $\hat{B}_0 = (657.99 \pm 0.15) \text{ meV/\AA}^3$ , the elastic constants are computed from the Equations 41 and 46.

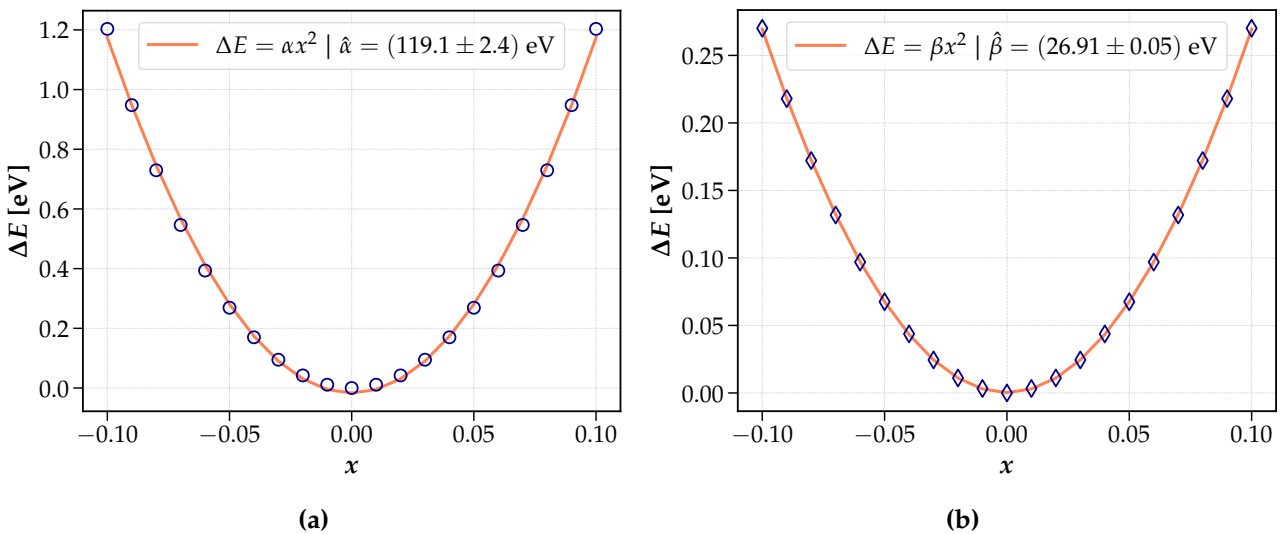


**Figure 9:** Energy variation as a function of strain used to determine the elastic constants. (a) Tetragonal deformation for extracting  $C_{11} - C_{12}$ , with symbols denoting computed energies and the solid curve showing the parabolic fit  $\Delta E = \alpha x^2$ . (b) Monoclinic deformation for extracting  $C_{44}$ , fitted similarly by  $\Delta E = \beta x^2$ . The best-fit parameters  $\hat{\alpha} = (119.1 \pm 2.4) \text{ eV}$  and  $\hat{\beta} = (26.91 \pm 0.05) \text{ eV}$  are obtained from non-linear least squares regression.

They are tabulated in Table 4 and compared with reference values. The associated uncertainties are estimated using standard error propagation based on the absolute values of the partial derivatives with respect to each parameter. Explicitly, the errors on the elastic constants are calculated as follows:

$$\begin{cases} \delta C_{11} = \left| \frac{\partial C_{11}}{\partial \hat{B}_0} \right| \delta \hat{B}_0 + \left| \frac{\partial C_{11}}{\partial \hat{\alpha}} \right| \delta \hat{\alpha} + \left| \frac{\partial C_{11}}{\partial V_0} \right| \delta V_0 = \delta \hat{B}_0 + \frac{2}{3} \left( \frac{\delta \hat{\alpha}}{V_0} + \frac{\hat{\alpha} \delta V_0}{V_0^2} \right), \\ \delta C_{12} = \delta \hat{B}_0 + \frac{1}{3} \left( \frac{\delta \hat{\alpha}}{V_0} + \frac{\hat{\alpha} \delta V_0}{V_0^2} \right), \\ \delta C_{44} = 2 \left( \frac{\delta \hat{\beta}}{V_0} + \frac{\hat{\beta} \delta V_0}{V_0^2} \right), \end{cases} \quad (47)$$

where  $\delta \hat{B}_0$ ,  $\delta \hat{\alpha}$ ,  $\delta \hat{\beta}$  and  $\delta V_0$  denote the uncertainties in the bulk modulus, the fitted parameter  $\hat{\alpha}$ , the fitted parameter  $\hat{\beta}$ , and the equilibrium volume, respectively.

**Comparison with references** The computed elastic constants  $C_{11} = (219 \pm 4)$  GPa,  $C_{12} = (49 \pm 3)$  GPa, and  $C_{44} = (76.9 \pm 0.5)$  GPa exhibit an overall agreement with theoretical and experimental values, as detailed in Table 4. For  $C_{11}$ , the computed value aligns well with both the experimental Brillouin scattering measurement ( $C_{11} = (219.4 \pm 0.7)$  GPa) [23] and the PP-DFT-B3LYP result ( $C_{11} = 219$  GPa) [17], with minimal relative errors of 0.2% and 0%, respectively. In contrast,  $C_{12}$  shows notable deviations from reference values, with relative errors spanning 14% to 26%. Its value is consistently lower than literature results. Such discrepancies may come from a greater sensitivity of  $C_{12}$  to the exchange-correlation functional approximation or pseudopotential treatment, as well as temperature effects in experimental data for instance. The  $C_{44}$  value demonstrates close agreement with DFT-GGA [19] and PP-PAW-GGA results, with relative errors of 1.2% and 5%, respectively.

| Elastic constants                    | $C_{11}$ [GPa]  |                             | $C_{12}$ [GPa] |                             | $C_{44}$ [GPa] |                             |
|--------------------------------------|-----------------|-----------------------------|----------------|-----------------------------|----------------|-----------------------------|
| Present work                         | $219 \pm 4$     |                             | $49 \pm 3$     |                             | $76.9 \pm 0.5$ |                             |
| References                           | $C_{11}$        | $\epsilon_{\text{rel}}$ [%] | $C_{12}$       | $\epsilon_{\text{rel}}$ [%] | $C_{44}$       | $\epsilon_{\text{rel}}$ [%] |
| Liu et al. (PP-PAW-GGA) [15]         | 215.1           | 1.8                         | 58.7           | 17                          | 78.4           | 1.9                         |
| Marinelli et al. (PP-DFT-PW) [17]    | 226             | 3                           | 57             | 14                          | 84             | 8                           |
| Marinelli et al. (PP-DFT-B3LYP) [17] | 219             | 0                           | 61             | 20                          | 86             | 11                          |
| Aguado et al. (AIM-MD) [18]          | 231.9           | 6                           | 58.2           | 16                          | 73.0           | 5                           |
| Deng et al. (DFT-GGA) [19]           | 215.1           | 1.8                         | 66.9           | 26                          | 77.8           | 1.2                         |
| Speziale et al. (BS) [23]            | $219.4 \pm 0.7$ | 0.2                         | $58.1 \pm 0.7$ | 15                          | $80.0 \pm 0.2$ | 4                           |

**Table 4:** Elastic constants computed from strain energy via DFT, with a norm-conserving pseudopotential. Values are compared with references including pseudopotential-projector augmented wave generalized gradient approximation (PP-PAW-GGA), Brillouin scattering (BS) experiments, all-electron DFT with B3LYP (AE-DFT-B3LYP), pseudopotential DFT with B3LYP (PP-DFT-B3LYP), and aspherical ion model molecular dynamics (AIM-MD) at room temperature.  $\epsilon_{\text{rel}}$  represent relative errors of the computed elastic constants with respect to the references.

## References

- [1] P. Hohenberg and W. Kohn. “Inhomogeneous Electron Gas”. In: *Phys. Rev.* 136 (3B Nov. 1964), B864–B871. DOI: [10.1103/PhysRev.136.B864](https://doi.org/10.1103/PhysRev.136.B864). URL: <https://link.aps.org/doi/10.1103/PhysRev.136.B864>.
- [2] Virah Sahni. *Quantal Density Functional Theory*. 2nd ed. Springer Berlin, Heidelberg, 2016, pp. XIX, 413. ISBN: 978-3-662-49840-8. DOI: <https://doi.org/10.1007/978-3-662-49842-2>.

- [3] W. Kohn and L. J. Sham. “Self-Consistent Equations Including Exchange and Correlation Effects”. In: *Phys. Rev.* 140 (4A Nov. 1965), A1133–A1138. DOI: [10.1103/PhysRev.140.A1133](https://doi.org/10.1103/PhysRev.140.A1133). URL: <https://link.aps.org/doi/10.1103/PhysRev.140.A1133>.
- [4] Julien Toulouse. *Introduction to density-functional theory*. Laboratoire de Chimie Théorique, Sorbonne Université and CNRS, Paris, France. Sept. 2024. URL: [https://www.lct.jussieu.fr/pagesperso/toulouse/enseignement/introduction\\_dft.pdf](https://www.lct.jussieu.fr/pagesperso/toulouse/enseignement/introduction_dft.pdf).
- [5] Nick Woods. *On the Nature of Self-Consistency in Density Functional Theory*. 2018. arXiv: [1803.01763](https://arxiv.org/abs/1803.01763) [cond-mat.other]. URL: <https://arxiv.org/abs/1803.01763>.
- [6] Ralph Gebauer. *Plane-Waves, pseudopotentials, k-points, FFTs ... and all that*. Advanced Workshop on High-Performance & High-Throughput Materials Simulations using Quantum ESPRESSO, ICTP, Trieste, Italy. Slides courtesy of Shobhana Narasimhan. Jan. 2017. URL: [https://www.materialscloud.org/learn/data/learn/files/B74aKUHPWg8E/1-2\\_Gebauer\\_Planewaves\\_Pseudopotentials.pdf](https://www.materialscloud.org/learn/data/learn/files/B74aKUHPWg8E/1-2_Gebauer_Planewaves_Pseudopotentials.pdf).
- [7] Hendrik J. Monkhorst and James D. Pack. “Special points for Brillouin-zone integrations”. In: *Phys. Rev. B* 13 (12 June 1976), pp. 5188–5192. DOI: [10.1103/PhysRevB.13.5188](https://doi.org/10.1103/PhysRevB.13.5188). URL: <https://link.aps.org/doi/10.1103/PhysRevB.13.5188>.
- [8] Wikimedia Commons. *File:Pseudopotential.png* — *Wikimedia Commons, the free media repository*. [Online; accessed 13-April-2025]. 2025. URL: <https://commons.wikimedia.org/w/index.php?title=File:Pseudopotential.png&oldid=997216778>.
- [9] D. R. Hamann, M. Schlüter, and C. Chiang. “Norm-Conserving Pseudopotentials”. In: *Phys. Rev. Lett.* 43 (20 Nov. 1979), pp. 1494–1497. DOI: [10.1103/PhysRevLett.43.1494](https://doi.org/10.1103/PhysRevLett.43.1494). URL: <https://link.aps.org/doi/10.1103/PhysRevLett.43.1494>.
- [10] David Vanderbilt. “Soft self-consistent pseudopotentials in a generalized eigenvalue formalism”. In: *Phys. Rev. B* 41 (11 Apr. 1990), pp. 7892–7895. DOI: [10.1103/PhysRevB.41.7892](https://doi.org/10.1103/PhysRevB.41.7892). URL: <https://link.aps.org/doi/10.1103/PhysRevB.41.7892>.
- [11] Paolo Giannozzi et al. “QUANTUM ESPRESSO: a modular and open-source software project for quantum simulations of materials”. In: *Journal of Physics: Condensed Matter* 21.39 (Sept. 2009), p. 395502. ISSN: 1361-648X. DOI: [10.1088/0953-8984/21/39/395502](https://doi.org/10.1088/0953-8984/21/39/395502). URL: <http://dx.doi.org/10.1088/0953-8984/21/39/395502>.
- [12] Peter Mohr et al. *CODATA Recommended Values of the Fundamental Physical Constants: 2022*. 2024. arXiv: [2409.03787](https://arxiv.org/abs/2409.03787) [hep-ph]. URL: <https://arxiv.org/abs/2409.03787>.
- [13] D. R. Hamann. “Optimized norm-conserving Vanderbilt pseudopotentials”. In: *Phys. Rev. B* 88 (8 Aug. 2013), p. 085117. DOI: [10.1103/PhysRevB.88.085117](https://doi.org/10.1103/PhysRevB.88.085117). URL: <https://link.aps.org/doi/10.1103/PhysRevB.88.085117>.
- [14] G. Fiquet, P. Richet, and G. Montagnac. “High-temperature thermal expansion of lime, periclase, corundum and spinel”. In: *Physics and Chemistry of Minerals* 27 (1999), pp. 103–111. DOI: [10.1007/s002690050246](https://doi.org/10.1007/s002690050246).
- [15] L. Liu, X.Z. Wu, R. Wang, et al. “High-pressure effect on elastic constants, stacking fault energy and correlation with dislocation properties in MgO and CaO”. In: *The European Physical Journal B* 85 (2012), p. 226. DOI: [10.1140/epjb/e2012-30032-4](https://doi.org/10.1140/epjb/e2012-30032-4). URL: <https://doi.org/10.1140/epjb/e2012-30032-4>.
- [16] Marie-Pierre Habas, Roberto Dovesi, and Albert Lichanot. “The phase transition in alkaline-earth oxides: a comparison of ab initio Hartree-Fock and density functional calculations”. In: *Journal of Physics: Condensed Matter* 10.31 (Aug. 1998), p. 6897. DOI: [10.1088/0953-8984/10/31/008](https://doi.org/10.1088/0953-8984/10/31/008). URL: <https://dx.doi.org/10.1088/0953-8984/10/31/008>.

- [17] F Marinelli and A Lichanot. “Elastic constants and electronic structure of alkaline-earth chalcogenides. Performances of various hamiltonians”. In: *Chemical Physics Letters* 367.3 (2003), pp. 430–438. ISSN: 0009-2614. DOI: [https://doi.org/10.1016/S0009-2614\(02\)01698-6](https://doi.org/10.1016/S0009-2614(02)01698-6). URL: <https://www.sciencedirect.com/science/article/pii/S0009261402016986>.
- [18] Andrés Aguado, Leonardo Bernasconi, and Paul A. Madden. “Interionic potentials from ab initio molecular dynamics: The alkaline earth oxides CaO, SrO, and BaO”. In: *The Journal of Chemical Physics* 118.13 (Apr. 2003), pp. 5704–5717. ISSN: 0021-9606. DOI: [10.1063/1.1556074](https://doi.org/10.1063/1.1556074). eprint: [https://pubs.aip.org/aip/jcp/article-pdf/118/13/5704/19289222/5704\\_1\\_online.pdf](https://pubs.aip.org/aip/jcp/article-pdf/118/13/5704/19289222/5704_1_online.pdf). URL: <https://doi.org/10.1063/1.1556074>.
- [19] Ye Deng et al. “Phase transition and elastic constants of CaO from first-principle calculations”. In: *Physica B: Condensed Matter* 392.1 (2007), pp. 229–232. ISSN: 0921-4526. DOI: <https://doi.org/10.1016/j.physb.2006.11.023>. URL: <https://www.sciencedirect.com/science/article/pii/S0921452606018424>.
- [20] E L Albuquerque and M S Vasconcelos. “Structural, electronics and optical properties of CaO”. In: *Journal of Physics: Conference Series* 100.4 (Mar. 2008), p. 042006. DOI: [10.1088/1742-6596/100/4/042006](https://doi.org/10.1088/1742-6596/100/4/042006). URL: <https://dx.doi.org/10.1088/1742-6596/100/4/042006>.
- [21] Tomoo Katsura and Yoshinori Tange. “A Simple Derivation of the Birch–Murnaghan Equations of State (EOSs) and Comparison with EOSs Derived from Other Definitions of Finite Strain”. In: *Minerals* 9.12 (2019). ISSN: 2075-163X. DOI: [10.3390/min9120745](https://doi.org/10.3390/min9120745). URL: <https://www.mdpi.com/2075-163X/9/12/745>.
- [22] Matthew Newville et al. *LMFIT: Non-Linear Least-Squares Minimization and Curve-Fitting for Python*. Version 1.3.3. Mar. 2025. DOI: [10.5281/zenodo.15014437](https://doi.org/10.5281/zenodo.15014437). URL: <https://doi.org/10.5281/zenodo.15014437>.
- [23] Sergio Speziale, Sean R. Shieh, and Thomas S. Duffy. “High-pressure elasticity of calcium oxide: A comparison between Brillouin spectroscopy and radial X-ray diffraction”. In: *Journal of Geophysical Research: Solid Earth* 111.B2 (2006). DOI: <https://doi.org/10.1029/2005JB003823>. eprint: <https://agupubs.onlinelibrary.wiley.com/doi/pdf/10.1029/2005JB003823>. URL: <https://agupubs.onlinelibrary.wiley.com/doi/abs/10.1029/2005JB003823>.
- [24] Yakov Itin. “Cauchy Relations in Linear Elasticity: Algebraic and Physics Aspects”. In: *Journal of Elasticity* 156.1 (Sept. 2023), pp. 39–77. ISSN: 1573-2681. DOI: [10.1007/s10659-023-10035-8](https://doi.org/10.1007/s10659-023-10035-8). URL: <http://dx.doi.org/10.1007/s10659-023-10035-8>.